First-principles Dynamics of Collisional Intersystem Crossing: Resonance Enhanced Quenching of C(1D) by N2

Journal:	*Physical Chemistry Chemical Physics*
Manuscript ID	CP-ART-11-2018-007171.R1
Article Type:	Paper
Date Submitted by the Author:	04-Jan-2019
Complete List of Authors:	An, Feng; Nanjing University, Han, Shanyu; Nanjing University, Chemistry Hu, Xixi; Nanjing University, School of Chemistry and Chemical Engineering Xie, Daiqian; Nanjing University, Department of Chemistry Guo, Hua; University of New Mexico, Department of Chemistry

Revised, 01/04/2019

First-principles Dynamics of Collisional Intersystem Crossing: Resonance Enhanced Quenching of $C(^1D)$ by N_2

Feng An,[1,#] Shanyu Han,[1,2,#] Xixi Hu,[1] Daiqian Xie,[1,*] and Hua Guo[2,*]

[1]*Institute of Theoretical and Computational Chemistry, Key Laboratory of Mesoscopic Chemistry, School of Chemistry and Chemical Engineering, Nanjing University, Nanjing 210023, China*

[2]*Department of Chemistry and Chemical Biology, University of New Mexico, Albuquerque, New Mexico, 87131, USA*

#: these authors contributed equally

*: corresponding authors: dqxie@nju.edu.cn, hguo@unm.edu

Abstract

Intersystem crossing is a common and important nonadiabatic process in molecular systems, and its first-principles characterization requires accurate descriptions of both the electronic structure and nuclear dynamics. Here, we report an accurate full-dimensional quantum dynamical investigation of collisional quenching of the excited state $C(^1D)$ atom to its ground state $C(^3P)$ counterpart by N_2, which is an important process in both combustion and interstellar media, using full-dimensional *ab initio* potential energy surfaces and spin-orbit couplings. Satisfactory agreement with experimental rate coefficients is obtained. Despite relatively small spin-orbit couplings, it is shown intersystem crossing is efficient because of multiple passage via long-lived collisional resonances.

I. Introduction

Electronic degeneracies, which are prevalent in molecular systems, break the Born-Oppenheimer adiabatic approximation and allow transitions between different electronic states. One special type of nonadiabatic processes is mediated by spin-orbit (SO) coupling, which facilitates spin-forbidden reactions[1] and photoreactions.[2] This so-called intersystem crossing (ISC) plays a prominent role in many molecular processes, particularly those involving heavy atoms because the SO coupling is a relativistic effect proportional to the fourth power of the atomic number. However, recent studies have demonstrated that ISC can also be quite facile for reactive systems involving light atoms, due apparently to dynamic effects.[3-5] To fully understand the dynamics of collisional ISC processes, a first-principles characterization of the potential energy surfaces (PESs) and their SO couplings, as well as the associated nonadiabatic dynamics, is needed. Unfortunately, most of the previous theoretical studies on such processes have been based on models with uncertainties in either the PESs or the nonadiabatic dynamics.[6-10] Thus far, very few first-principles studies have been reported, largely due to the complications associated with both the ab initio determination of the full-dimensional PESs and SO coupling and/or quantum mechanical characterization of the nuclear dynamics.[11-13] In this publication, we focus on a prototypical collisional ISC process, namely the quenching of $C(^1D)$ to $C(^3P)$ by N_2, which is amenable to such a thorough quantum mechanical treatment.

Atomic carbon is present in abundance in combustion, atmospheres, and interstellar media. It is well established that the ground state carbon atom, $C(^3P)$, is in general much less reactive than its excited counterpart, $C(^1D)$.[14] The quenching of $C(^1D)$ to $C(^3P)$ by N_2 is believed to exist in robust nitrogen atmospheres, such as those of Earth and Titan. As a result, the quenching reaction may compete with reactive processes if the corresponding rates are comparable.[15] Early experimental studies of the quenching reaction were reported in 1969 by Braun *et al*.,[16] who indirectly monitored the pertinent species to measure the rate coefficient using a vacuum ultraviolet photolysis method at room-temperature. In 1971, Husain and Kirsch remeasured the room-temperature rate coefficient with a direct method.[17] In 2016, Hickson *et al.* reported the low-temperature quenching rate coefficient using vacuum ultraviolet laser-induced fluorescence with a supersonic flow reactor.[15] The results suggested that the quenching rate increases with decreasing temperature, suggesting a prominent role of this ISC process in low-temperature environments.

Theoretically, several *ab initio* studies of the CN_2 free radical have been reported,[18-25] but three-dimensional PESs for the quenching process are still absent. In an effort to understand the quenching dynamics, one-dimensional potential energy curves for eight electronic states of CN_2 at collinear and perpendicular (C_{2v}) geometries were computed by Hickson *et al.*[15] These authors then computed the rate coefficients using spherically averaged potentials with a SO coupling matrix.[15] Because of the severe approximations in that model, their theoretical rate coefficients only provided a qualitative characterization of the quenching process.

In this publication, we focus on the following process

$$C(^1D) + N_2(v = 0, j = 0) \rightarrow C(^3P) + N_2(v', j') . \quad \text{(R1)}$$

We report the construction of accurate three-dimensional PESs of several low-lying electronic states of the system and the corresponding SO coupling surfaces by fitting a large number of high-level *ab initio* points. The nonadiabatic quenching dynamics are investigated using a wave packet method for a range of collision energies, E_c=0.001~0.500 eV. The cross sections and rate coefficients are computed and compared with the available experimental results. In agreement with experiment, the quenching rate increases with decreasing temperature at moderately low temperatures between 300 and 50 K. The efficient non-adiabatic quenching cross section is attributed to long-lived resonances supported by the PESs, which allow multiple passes of the crossing seams. This theoretical study thus sheds light on the ISC process in this important prototype. The remainder of the publication is organized as follows. The next section (Sec. II) discusses the theoretical methods for treating the ISC dynamics in this system, including the definition of representations, the derivation of Hamiltonians, the ab initio calculations and fitting of the PESs and SO coupling surfaces, as well as the nonadiabatic nuclear dynamics on the coupled PESs. The results are presented and discussed in Sec. III. The final section (Sec. IV) concludes.

II. **Theory**

II-A. Representations

The five electronic states involved in the quenching are $1^1A'$, $1^1A''$, $1^3A'$, $1^3A''$, and $2^3A''$ in C_s symmetry. The electronic orbital momentum quantum number and its projection onto the molecular axis are denoted as l and λ, respectively. The latter is a good quantum number at linear configurations. At linearity, the $1^1A'$ and $1^1A''$ states form a degenerate pair labeled as $^1\Delta$ with $|\lambda|=2$, while the $1^3A'$ and $2^3A''$ states are two degenerate components of the $^3\Pi$ state with $|\lambda|=1$. The remaining $1^3A''$ state, the ground state, is represented in linearity by $^3\Sigma^-$ which has $\lambda=0$. Below, we only consider the positive values of λ. These states are eigenstates of the electronic Hamiltonian matrix $\hat{H}_{el}$.These adiabatic states can be denoted by the following new symbols as: $\left|1^1A'\right\rangle \equiv \left|{}^1\Delta_{x^2-y^2}\right\rangle$, $\left|1^1A''\right\rangle \equiv \left|{}^1\Delta_{xy}\right\rangle$, $\left|1^3A'\right\rangle \equiv \left|{}^3\Pi_x\right\rangle$, $\left|2^3A''\right\rangle \equiv \left|{}^3\Pi_y\right\rangle$, $\left|1^3A''\right\rangle \equiv \left|{}^3\Sigma^-\right\rangle$.[15] Depending on the λ discussed above, we can also define signed-λ diabatic basis, $\left|{}^1\Delta_2\right\rangle$, $\left|{}^1\Delta_{-2}\right\rangle$, $\left|{}^3\Pi_1\right\rangle$, $\left|{}^3\Pi_{-1}\right\rangle$ and $\left|X^3\Sigma^-\right\rangle$. The relation between signed-λ basis and adiabatic basis can be found in Ref. 26.

When the SO coupling is considered, new bases with explicit inclusion of spin have to be used. Following Alexander and coworkers,[27, 28] a diabatic representation denoted as $\left|\lambda\sigma\right\rangle$ is preferred for deriving the electronic Hamiltonian matrix $\hat{H}_{el}$ and SO coupling Hamiltonian matrix $\hat{H}_{so}$, which is defined by λ-signed basis and spin projection. Here, λ is conveniently assumed to still be a good quantum number even for nonlinear configurations. For the spin, σ is the magnetic spin quantum number, which is the projection of the total spin angular momentum (s) on to the z axis. This basis are formally the eigenfunctions of both $\hat{l}^2$, $\hat{l}_z$, $\hat{s}^2$, and $\hat{s}_z$ operators ($\hbar$=1 hereafter):

$$\hat{l}^2\left|\lambda\sigma\right\rangle = l(l+1)\left|\lambda\sigma\right\rangle,\ \hat{l}_z\left|\lambda\sigma\right\rangle = \lambda\left|\lambda\sigma\right\rangle, \quad (1)$$

$$\hat{s}^2\left|\lambda\sigma\right\rangle = s(s+1)\left|\lambda\sigma\right\rangle,\ \hat{s}_z\left|\lambda\sigma\right\rangle = \sigma\left|\lambda\sigma\right\rangle. \quad (2)$$

For a singlet (triplet) electronic state, the spin angular momentum quantum numbers are s=0, σ=0 (s=1, σ=0, ±1). Thus for CN_2, there are eleven diabatic basis, which are denoted as $\left|^3\Pi_1;+1\right\rangle$, $\left|^1\Delta_2;0\right\rangle$, $\left|^3\Pi_{-1};-1\right\rangle$, $\left|^1\Delta_{-2};0\right\rangle$, $\left|^3\Sigma^-;0\right\rangle$, $\left|^3\Pi_1;-1\right\rangle$, $\left|^3\Pi_{-1};+1\right\rangle$, $\left|X^3\Sigma^-;+1\right\rangle$, $\left|^3\Pi_1;0\right\rangle$, $\left|X^3\Sigma^-;-1\right\rangle$ and $\left|^3\Pi_{-1};0\right\rangle$, in the $\left|^{2s+1}l_\lambda;\sigma\right\rangle$ form.

II-B. The Hamiltonians

At linear configurations, the projection of the electronic total angular momentum onto the molecular axis is denoted by $|\omega=l+s|$. By integrating over the electronic coordinates, one can define the elements of the diabatic potential energy matrix (PEM):

$$\left\langle\lambda'\sigma'\right|\hat{H}_{el}\left|\lambda\sigma\right\rangle = \delta_{\sigma\sigma'}V_{\lambda'\lambda}, \quad (3)$$

and

$$\left\langle\lambda'\sigma'\right|\hat{H}_{so}\left|\lambda\sigma\right\rangle = W_{\lambda'\sigma'\lambda\sigma}. \quad (4)$$

In this representation, only couplings between the states with the same σ and $|\lambda|$ are non-vanishing, as suggested in eqn. (3). Furthermore, couplings between states with different $|\omega = \lambda + \sigma|$ values vanish, as shown in eqn. (4), due to the selection rules of SO coupling.[27-29]

At C_{2v} configurations, there is a conical intersection (CI) between the $^3A_2$ ($1^3A''$) and $^3B_1$($2^3A''$) states, but their effects are ignored, as advocated by Hickson *et al.*[15] as the minimum energy crossing (MEX) of the CI is about 0.7 eV higher than the

$C(^1D) + N_2$ asymptote (R=8.00 Å). Our value for the MEX (R=1.32 Å, r=1.27 Å, and γ=90°) is 0.62 eV higher than the $C(^1D) + N_2$ asymptote. Furthermore, the $^1\Delta$ ($1^1A'$ and $1^1A''$, ω=2) to $^3\Sigma^-$($1^3A''$, ω=0) ISC channel is not considered, because the corresponding SO coupling is much smaller than that between the $^1\Delta$($1^1A'$ and $1^1A''$, ω=2) and $^3\Pi$($1^3A'$and $2^3A''$, ω=2) states. This recognizes the latter as the dominant ISC quenching pathway. The couplings between states with $|\omega| = 1$ and others are also small and are thus neglected in our dynamic models. With these approximations, we can simplify the model by one with only six diabatic states ($\left|{}^3\Pi_1;+1\right\rangle$, $\left|{}^1\Delta_2;0\right\rangle$, $\left|{}^3\Pi_{-1};-1\right\rangle$, $\left|{}^1\Delta_{-2};0\right\rangle$, $\left|{}^3\Pi_1;-1\right\rangle$ and $\left|{}^3\Pi_{-1};+1\right\rangle$), in which the electronic Hamiltonian matrix can be represented as eqn. (3) in Table I. The matrix elements ($V_\Pi \equiv V_{\pm1,\pm1}$, $V_\Delta \equiv V_{\pm2,\pm2}$, $V_1 \equiv V_{\pm1,\mp1}$, $V_2 \equiv V_{\pm2,\mp2}$) in Table I can be obtained from the adiabatic energies obtained from *ab initio* calculations. In particular, we have

$$V_\Pi = \frac{V_{xx} + V_{yy}}{2}, \tag{5}$$

$$V_\Delta = \frac{V_{x^2-y^2} + V_{xy}}{2}, \tag{6}$$

$$V_1 = \frac{V_{yy} - V_{xx}}{2}, \tag{7}$$

$$V_2 = \frac{V_{x^2-y^2} - V_{xy}}{2}, \tag{8}$$

where

$$V_{xx} = \left\langle {}^3\Pi_x \left| \hat{H}_{el} \right| {}^3\Pi_x \right\rangle, \tag{9}$$

$$V_{yy}=\left\langle {}^3\Pi_y \left| \hat{H}_{el} \right| {}^3\Pi_y \right\rangle, \tag{10}$$

$$V_{x^2-y^2}=\left\langle {}^1\Delta_{x^2-y^2} \left| \hat{H}_{el} \right| {}^1\Delta_{x^2-y^2} \right\rangle, \tag{11}$$

$$V_{xy}=\left\langle {}^1\Delta_{xy} \left| \hat{H}_{el} \right| {}^1\Delta_{xy} \right\rangle. \tag{12}$$

The matrix of the SO Hamiltonian in the $\left|\lambda\sigma\right\rangle$ basis is given by eqn. (4) in Table II. The selection rules are $\Delta\lambda=\Delta\sigma=0$ and $\Delta s=0$ or $\Delta s=\pm1$ for the $\hat{l}_z\cdot\hat{s}_z$ operator or $\Delta\lambda=\pm1,\Delta\sigma=\mp1$ for the $1/2\cdot(\hat{l}_+\cdot\hat{s}_-+\hat{l}_-\cdot\hat{s}_+)$ operator between different basis states with same signed value of ω.[27,29] The SO coupling elements A ($W_{\pm1,\pm1,\pm1,\pm1}$), C ($W_{\pm1,\pm1,\pm2,0}$) and E ($W_{\pm1,m1,\pm1,m1}$) are defined as

$$A=i\left\langle {}^3\Pi_x;+1\left| \hat{H}_{so} \right| {}^3\Pi_y;+1\right\rangle, \tag{13}$$

$$C=-\frac{1}{2}(C_1+C_2+C_3+C_4), \tag{14}$$

where

$$C_1=\left\langle {}^3\Pi_x;+1\left| \hat{H}_{so} \right| {}^1\Delta_{x^2-y^2};0\right\rangle, \tag{15}$$

$$C_2=\left\langle {}^3\Pi_y;+1\left| \hat{H}_{so} \right| {}^1\Delta_{xy};0\right\rangle, \tag{16}$$

$$C_3=-i\left\langle {}^3\Pi_y;+1\left| \hat{H}_{so} \right| {}^1\Delta_{x^2-y^2};0\right\rangle, \tag{17}$$

$$C_4=i\left\langle {}^3\Pi_x;+1\left| \hat{H}_{so} \right| {}^1\Delta_{xy};0\right\rangle, \tag{18}$$

and

$$E=i\left\langle {}^3\Pi_x;-1\left| \hat{H}_{so} \right| {}^3\Pi_y;-1\right\rangle. \tag{19}$$

Because the off-diagonal energy difference V_1 and V_2 are relatively small along the minimum energy pathway near linearity, where the Π and Δ states are doubly

degenerate, this model can be further simplified to involve only two states ($\left|{}^3\Pi_{\pm1};\pm1\right\rangle$ and $\left|{}^1\Delta_{\pm2};0\right\rangle$). In an earlier study of the SO coupled dynamics of the Cl + H_2 reaction, it has been shown a similar simplification is justified and yield good results.[28, 30] Hence, a reduced two-state model is used here to treat the nonadiabatic dynamics, which has the combined Hamiltonian ($\hat{H}_{so}+\hat{H}_{el}$) in Table III.

II-C. *Ab initio* calculations and fitting of PESs

The *ab initio* electronic structure calculations for constructing PESs of the CN_2 system were carried out using the MOLPRO package.[31] The molecular orbitals (MOs) were determined by the state-averaged complete active space self-consistent field (SA-CASSCF)[32, 33] calculations including eight states ($1^1A'$, $2^1A'$, $3^1A'$, $1^1A''$, $2^1A''$, $1^3A'$, $1^3A''$, and $2^3A''$ in C_s symmetry), with the full-valence active space involving 20 electrons in 15 occupied orbitals. The 1s orbitals of the C and N atoms were doubly occupied in all configurations and not optimized. The correlation-consistent polarized valence triple-zeta with explicitly correlated basis set (cc-pVTZ-F12)[34] was used. The explicitly correlated and internally contracted multi-reference configuration interaction method with the Davidson correction (MRCI-F12+Q)[35] was finally used in the *ab initio* calculations.

About 2000 geometries were generated in the Jacobi coordinates (R, r, γ) where R is the distance between C and the N_2 center of mass, r the N-N distance, and γ the Jacobi angle. These points were chosen from the following ranges: $R \in$ (0, 8.00 Å), $r \in$ (0.95, 3.00 Å), and $\gamma \in$ (0 to 90°). The adiabatic PESs of the five lowest electronic

states ($1^1A'$, $1^1A''$, $1^3A'$, $1^3A''$, and $2^3A''$ in C_s symmetry) are obtained at these geometries. The SO coupling matrix elements are computed by using the Breit-Pauli Hamiltonian at the CASSCF level.[32, 33]

To provide an analytical representation of the *ab initio* points, the permutation invariant polynomial-neural network (PIP-NN) method[36, 37] was used in fitting. In the PIP-NN method, the NN is frontloaded with low-order PIPs to enforce the permutation symmetry of the two N atoms. The PIPs are the symmetrized monomials of the Morse like variables designed as[38]

$$p_{ij} = e^{-\frac{r_{ij}}{a}}, \tag{20}$$

where r_{ij} represents the internuclear distance between the *i*th and *j*th atoms and a is set to 2.0 bohr in this work. For CN_2, the following first order PIPs were used:[38]

$$G_1 = \frac{p_{13} + p_{23}}{2},\ G_2 = p_{13}p_{23},\ G_3 = p_{12}, \tag{21}$$

where the N, N, and C atoms are labeled as 1, 2, and 3, respectively. The PIP-NN method has been quite successful in constructing high fidelity global PESs for small systems.[39]

In this work, the standard feed-forward NN is constructed with $\{G_i\}$ being the input layer. The *ab initio* points are randomly divided into training (90%), validation (5%), and testing sets (5%), respectively. The NNs are trained using the Levenberg-Marquardt algorithm with early stopping for avoiding overfitting and the root mean square errors (RMSEs), defined as

$$\mathrm{RMSE} = \sqrt{\sum_{i=1}^{N} \frac{(E_{output} - E_{target})^2}{N}} \tag{22}$$

is used to measure the performance. E_{target} and E_{output} are the energy of input data and the fitted one, respectively.

The SO matrix elements were fitted using PIP-NN method with the same PIPs used in the PES fitting.

II-D. Nonadiabatic dynamics

The Hamiltonian in the C-N_2 Jacobi coordinates (R, r, γ) is given by

$$\hat{H} = -\frac{1}{2\mu_R}\frac{\partial^2}{\partial R^2} - \frac{1}{2\mu_r}\frac{\partial^2}{\partial r^2} + \frac{\hat{L}^2}{2\mu_R R^2} + \frac{\hat{j}^2}{2\mu_r r^2} + \hat{H}_{el} + \hat{H}_{so}. \tag{23}$$

where the first two terms denote the radial kinetic energy operators for R (C-N_2 distance) and r (N-N distance), with μ_R and μ_r as the reduced masses. $\hat{L}$ is the orbital angular momentum operator and $\hat{L}^2$ can be written as $(\hat{J} - \hat{j})^2$, in which we ignore the electronic and spin angular momenta ($\hat{l}$ and $\hat{s}$), following Alexander *et al*,[28] in two-state model calculations. The total angular momentum and diatomic rotational angular momentum are denoted as $\hat{J}$ and $\hat{j}$, respectively. We further neglect the Coriolis coupling between total $\hat{J}$, $\hat{l}$, and $\hat{s}$, which couples different ω states.[27] The last two terms are the electronic and SO Hamiltonians, which have been given above. Ignoring the Coriolis coupling between different spin states in addition to the approximations made in $\hat{H}_{el}$ and $\hat{H}_{so}$, the nonadiabatic dynamics in the C(^{1}D) + N_2 intersystem crossing can be described by a two-state model in which quenching happens only via

off-diagonal terms in $\hat{H}_{so}$. In our model, we define the *z*-axis of the BF frame along the $\vec{R}$ vector, and the CN_2 molecule is placed in the *x*-*z* plane. The rotation between the BF and space-fixed (SF) frames is defined by three Euler angles (ϕ, θ, χ).

In the diabatic representation, the total wavefunction with a total angular momentum *J* and parity *p* is expressed as

$$\left|\psi^{Jp}\right\rangle = \sum_{\alpha_1\alpha_2 j\Omega} \psi^{Jp}_{\alpha_1\alpha_2 j\Omega} \left|\alpha_1\alpha_2\right\rangle \left| j\Omega; JMp\right\rangle \left|\lambda\sigma\right\rangle, \tag{24}$$

in which α_1 and α_2 denote the indices of the radial grids, respectively. The parity-adapted angular basis is defined below

$$\left| j\Omega; JMp\right\rangle = [2(1+\delta_{\Omega,0})]^{-1/2} \sqrt{\frac{2J+1}{8\pi^2}} \left[D^{J*}_{\Omega,M} \Theta_{j\Omega}(\gamma) + p(-1)^J D^{J*}_{-\Omega,M} \Theta_{j-\Omega}(\gamma) \right]. \tag{25}$$

Here, $D^J_{\Omega,M}$ is a Wigner rotation matrix element, where *J* designates the total angular momentum with SF projection *M* and BF projection Ω, and $\Theta_{j\Omega}(\theta)$ are normalized associate Legendre functions with the Condon-Shortley phase convention where *j* designates the diatomic angular momentum.

The Chebyshev propagator[40] is employed to propagate the wave packet as

$$\Psi_{n+1} = 2D\hat{H}\Psi_n - D^2\Psi_{n-1} (n \geq 1), \tag{26}$$

where $\Psi_1 = D\hat{H}\Psi_0$ and Ψ_0 is the initial wavefunction. *D* is the damping function that prevents reflection at the edges of the grid. The radial kinetic energy operator is represented by sinc-DVR,[41] and the angular kinetic energy operator by FBR.[42] The action of the potential energy operator is evaluated in a grid via a unitary transformation

between the FBR and DVR.[43] Time-dependent quantities can be readily obtained from the Chebyshev domain, as shown by Tal-Ezer and Kosloff.[44]

The *S*-matrix elements were calculated by cosine Fourier transforming the Chebyshev correlation functions in the BF frame and then transformed into the SF frame.[45] By summing over the initial and final orbital angular momentum quantum numbers L_0 and L_f, the quenching state-to-state integral cross section (ICS) from different initial ro-vibrational (v_0, j_0) states of N_2 to its different final (v_f, j_f) states can be written as

$$\sigma_{v_f j_f \leftarrow v_0 j_0}(E_c) = \frac{\pi}{(2j_0+1)k_{v_0 j_0}^2} \sum_{Jp} \sum_{L_f} \sum_{L_0} (2J+1) \left| S^{Jp}_{v_f j_f L_f \leftarrow v_0 j_0 L_0}(E) \right|^2 , \qquad (27)$$

where $k_{v_0 j_0} = \sqrt{2\mu_R E_c}$ and E_c is the collision energy. The uniform *J*-shifting approach[46, 47] was used in ICS calculations. The initial state-specified rate coefficient with summing up all probable final ro-vibrational states was obtained by Boltzmann-averaging the corresponding ICS over the collision energy (E_c) as

$$k(T) = \frac{q^{\neq}}{Q_{el}} \frac{1}{k_B T} \sqrt{\frac{8}{\pi \mu_R k_B T}} \int_0^{\infty} \sum_{v_f j_f} \sigma_{v_f j_f \leftarrow v_0 j_0}(E_c) e^{-E_c / k_B T} E_c dE_c , \qquad (28)$$

where k_B is the Boltzmann constant, T is the temperature. In the quenching reaction, the electronic partition function Q_{el} equals five accounting for the five-fold degeneracy of C(^{1}D) and the degeneracy of the electronic state $q^{\neq}$ equals 2.[48]

III. Results and Discussion

A. Potential energy surfaces and SO couplings

The total RMSEs of five PESs are 5.0, 5.9, 9.6, 8.7, and 8.5 meV, respectively. The RMSEs for the SO coupling *A* and *C* are 0.021 and 0.023 meV, respectively. The fitting errors suggest that both the diagonal and off-diagonal elements of the potential energy matrix are well represented.

The potential energy curves for the collinear approach of the atom C to the molecule N_2 are shown in Fig. 1(a). The triplet states $^3\Pi$ (doubly degenerate) and $^3\Sigma^-$ are correlated to the $C(^3P)+N_2(^1\Sigma_g^+)$ asymptote, while the singlet states $^1\Delta$ (doubly degenerate) are correlated to the $C(^1D)+N_2(^1\Sigma_g^+)$ asymptote. All three PESs have wells, corresponding to the collinear CNN radical. There is a significant barrier for the $^3\Pi$ state. In Fig. 1(b), the potential energy curves for the perpendicular (C_{2v}) approach of the C atom to the molecule N_2 are shown. The $^3\Pi$ and $^1\Delta$ states, which are degenerated in collinear configurations, now split into the $^3B_1$ and $^3B_2$ states, and to the $^1A_1$ and $^1A_2$ states, respectively.

The calculated equilibrium geometries the collinear CNN radical at the three lowest-lying electronic states are shown in Table IV. The agreement with the previous theoretical values,[15] which are also listed in the table for comparison, is quite reasonable. In Table V, the calculated adiabatic excitation energy is compared with the earlier theoretical[15, 21] and experimental values.[18] The comparison is also quite satisfactory. The calculated dissociation energy (D_e) of CNN on the ground state to the $C(^3P)+N_2(^1\Sigma_g^+)$ asymptote is calculated to be 32.6 kcal/mol, which is almost identical to the value reported by Hickson *et al*. (32.5 kcal/mol).[15] Experimentally, Clifford *et*

al.[18] estimated the D_0 value to be 37±3 kcal/mol. Our D_0 value is 31.4 kcal/mol, which is in qualitative agreement with the experiment. The singlet-triplet gap for the carbon atom is 10023.8 cm^{-1}, which agrees with the 10000 cm^{-1} value reported by Hickson *et al.*[15] These values can be compared with 10192.6 cm^{-1} from NIST Atomic Spectra Database.[49]

The contours of the $V_{^3\Pi}$ and $V_{^1\Delta}$ PESs are shown in the lower panels of Fig. 1. Here, the energy zero is defined at the equilibrium geometry of CNN ground state. It is clear from Fig. 1(c) that the triplet state is largely repulsive as the two reactants approach each other. At linear geometry, there is a high energy barrier, but the ISC crossing seam occurs before the barrier. In Fig. 1(d), it is shown that the singlet state is attractive in the collinear geometry, featuring a deep well near R is about 1.8 Å. However, it becomes repulsive in the perpendicular path. From these contour plots, it is clear that the PESs are quite anisotropic. Consequently, the treatment of N_2 as a sphere, as done in the previous work,[15] is bound to introduce large errors.

In Fig. 2, the SO matrix elements A and C (cm^{-1}) are shown as a function of each (R, γ) with the r(N-N) distance at 1.183 Å. The element A representing the diagonal SO coupling between $\left|{}^3\Pi_1;+1\right\rangle$ and $\left|{}^3\Pi_1;+1\right\rangle$ is shown at upper panel. The element C representing the off-diagonal SO coupling between $\left|{}^3\Pi_1;+1\right\rangle$ and $\left|{}^1\Delta_2;0\right\rangle$ is shown in lower panel. At the collinear crossing seam (R=2.67Å), they are very small (A = 11.60cm^{-1}, C = -23.56cm^{-1}).

To test the SO coupling, the splitting among the three fine-structure states of ground state carbon, namely the $^3P_2$, $^3P_1$, and $^3P_0$ states, are computed by diagonalizing $\hat{H}_{el} + \hat{H}_{so}$ as

$$\left\langle {}^3\mathrm{P}_n \left| \hat{H}_{el} + \hat{H}_{so} \right| {}^3\mathrm{P}_n \right\rangle = E_n \qquad n = 0,1,2 \tag{29}$$

using the SO coupling elements at the asymptotic collinear geometry for CNN with N_2 in the equilibrium geometry. The comparison with experimental values suggest that the calculated SO couplings lead to underestimation of the experimental energies, as shown in Table VI. As a result, these elements are multiplied by a factor of 1.213 to scale *A* and *C* in the $\hat{H}_{so}$ matrix in the calculations reported below. The fine-structure energy levels using the scaled *A* and *C* are given in parentheses, and their agreement with experiment is much better.

B. Quenching dynamics

To compute the quenching probabilities, a Gaussian wave packet is launched form the reactants C(^{1}D) and N_2 (*R*=12.00 bohr). The central collision energy and width of the initial wave packet are respectively 0.10 eV and 0.10 bohr, and it is associated with the ground rovibrational state of N_2. The calculations were carried out using a rovibrational basis with v_{max} = 6 and the j_{max} = 128 and its corresponding DVR grid. The propagation time is 19 ps, which is sufficient to converge the dynamical results. A damping function of the form $\exp(-0.3\Delta_t[(R-13.00)/5.00]^2)$, 13.00 bohr $\leq R \leq$ 18.00 bohr, was used in the *R* coordinate to impose outgoing boundary conditions. To make the rate coefficient converged at temperatures below 300 K, the collision energy should

be up to 0.50 eV and the maximum J value would be up to 130. The J-shift method was for J values higher than 21, while for J values between 0 and 20 the cubic spline interpolation method was used with the results for J = 0, 5, 10, 15, and 20.

The quenching reaction probabilities are plotted in Fig. 3 for several partial waves. It is clear from the J=0 result, that there is hardly any threshold, indicating a barrierless process. This is consistent with the fact that the crossing seam near the collinear geometry between the $^1\Delta$ and $^3\Pi$ states near R=2.67 Å is 0.10 eV lower than the $C(^1D)+N_2(^1\Sigma_g^+)$ asymptote. A threshold starts to appear for higher J values, due apparently to the centrifugal barrier. At low collision energies, the probabilities generally decay with increasing energy, suggestive of a capture process. Most prominently, the reaction probabilities are dominated by many oscillatory features, which are due to long-lived resonances. These resonances are mostly supported by the collinear well of the $^1\Delta$ state. In Figure 4, the resonance wavefunction in the $^1\Delta$ state at E_c=0.284 eV above the $C(^1D)+N_2(^1\Sigma_g^+)$ asymptote is plotted over the PES contours at the collinear geometry. It can be seen from the figure that the wavefunction is largely localized in the PES well and has with many nodes. Resonances like this are above the $C(^3P)+N_2(^1\Sigma_g^+)$ asymptote and their decay is via ISC to the $^3\Pi$ state. Due to their long lifetimes, evidenced by the narrow widths in the reaction probabilities, the ISC occurs via repeated passage of the crossing seam. Despite small SO coupling, the multiple passage of the crossing seam greatly enhances the ISC process, leading to efficient quenching.

The N_2 vibrational and rotational state distributions at J=0 are displayed in Fig. 5 for several collision energies. The N_2 vibration is mostly below v=2, but there are also some population at higher levels (v=4). The former can be attributed to the small variation of the N-N distance in both PESs. On the other hand, the latter is most likely due to resonance energy transfer as the energy of $N_2(v=4)$ is very close to the $C(^1D)+N_2(^1\Sigma_g^+)$ asymptote. The rotation of N_2 is highly excited, with j up to 60. The rotational excitation is most likely due to the anisotropy of the PESs, which exerts a torque on the N_2 moiety during the collision. Since not all partial waves are computed explicitly, no cross sections were obtained.

Finally, the calculated quenching rate coefficient is plotted in Fig. 6 as a function of temperature, along with the available experimental data. The earlier theoretical results of Hickson *et al*.[15] are also included for comparison. It can be seen that our calculated rate coefficients are in much better agreement with experiment, capturing more than 30% of the measured values, than either the collinear or spherical models used in Ref. [15]. More importantly, our results clearly reproduced the negative temperature dependence of the rate coefficient, which is almost certainly due to the monotonically decaying reaction probabilities at small J values. This trend was not captured in previous theoretical calculations. The remaining error in our calculations could be due to a number of reasons. For instance, the internally excited N_2 reactant, which are not considered in this work, might enhance the quenching. The neglect of derivative coupling and conical intersections might also cause uncertainty. In addition,

errors in ab initio calculations and fitting cannot be completely ruled out as well. Finally, the dynamic approximations discussed above could introduce additional errors.

III. Conclusions

In this work, we constructed the full-dimensional PESs for three triplet states and two singlet states of CN_2 using the PIP-NN fitting method. The *ab initio* calculations used in these fittings are performed at the ic-MRCI-F12+Q level with the cc-pVTZ-F12 basis set. The equilibrium geometries and excited energies are in good agreement with previous theoretical and experimental results. And two SO coupling elements *A* and *C* are calculated at CASSCF level with cc-pVTZ-F12 basis set and fitted by PIP-NN approach. The small RMSEs of those surfaces are indicative of high-fidelity representation of the *ab initio* data.

The quenching dynamics is investigated using a diabatic representation with an effective two-state model. To this end, the quenching probabilities were computed for several *J* values using a full-dimensional Chebyshev wave packet method. The quenching at J=0 has no threshold, and the probabilities decay as a function of the collision energy at low energies. This suggests that the ISC quenching resembles a barrierless capture process, which manifests in the rate coefficient as the negative temperature dependence, in agreement with experiment. The quenching is enhanced by long-lived resonances, which allow multiple passage the ISC crossing seam. The calculated rate coefficients are in satisfactory agreement with experiment, within a

factor of 2-3. This full-scale quantum dynamical study shed valuable light on the mechanism of collisional ISC processes.

ACKNOWLEDGMENTS: This work is supported by the Ministry of Science and Technology (2017YFA0206501 to D. X.), the National Natural Science Foundation of China (Grant Nos. 21733006, 21590802, and 91641104 to D.X.), and by United States Department of Energy (Grant No. DE-SC0015997 to H.G.).

References:

1. J. N. Harvey, *Phys. Chem. Chem. Phys.*, 2007, **9**, 331.
2. C. M. Marian, *WIREs: Comput. Mol. Sci.*, 2012, **2**, 187.
3. F. Leonori, A. Occhiogrosso, N. Balucani, A. Bucci, R. Petrucci and P. Casavecchia, *J. Phys. Chem. Lett.*, 2012, **3**, 75.
4. B. Fu, Y.-C. Han, J. M. Bowman, L. Angelucci, N. Balucani, F. Leonori and P. Casavecchia, *Proc. Natl. Acad. Sci. U. S. A.*, 2012, **109**, 9733.
5. H. Li, A. Kamasah, S. Matsika and A. G. Suits, *Nat. Chem.*, 2018.
6. J. B. Delos, *J. Chem. Phys.*, 1973, **59**, 2365.
7. G. E. Zahr, R. K. Preston and W. H. Miller, *J. Chem. Phys.*, 1975, **62**, 1127.
8. H. Tachikawa, T. Hamabayashi and H. Yoshida, *J. Phys. Chem.*, 1995, **99**, 16630.
9. H. Tachikawa, K. Ohnishi, T. Hamabayashi and H. Yoshida, *J. Phys. Chem. A*, 1997, **101**, 2229.
10. T. Takayanagi, *J. Phys. Chem. A*, 2002, **106**, 4914.
11. H. Nakamura and S. Kato, *J. Chem. Phys.*, 1999, **110**, 9937.
12. T.-S. Chu, T.-X. Xie and K.-L. Han, *J. Chem. Phys.*, 2004, **121**, 9352.
13. P. Defazio, P. Gamallo and C. Petrongolo, *J. Chem. Phys.*, 2012, **136**, 054308.
14. R. J. Donovan and D. Husain, *Chem. Rev.*, 1970, **70**, 489.
15. K. M. Hickson, J.-C. Loison, F. Lique and J. Kłos, *J. Phys. Chem. A*, 2016, **120**, 2504.
16. W. Braun, A. M. Bass, D. D. Davis and J. D. Simmons, *Proc. Royal Soc. A*, 1969, **312**, 417.
17. D. Husain and L. J. Kirsch, *Chem. Phys. Lett.*, 1971, **9**, 412.
18. E. P. Clifford, P. G. Wenthold, W. C. Lineberger, G. A. Petersson, K. M. Broadus, S. R. Kass, S. Kato, C. H. DePuy, V. M. Bierbaum and G. B. Ellison, *J. Phys. Chem. A*, 1998, **102**, 7100.
19. J. M. L. Martin, P. R. Taylor, J. P. François and R. Gijbels, *Chem. Phys. Lett.*, 1994, **226**, 475.
20. L. V. Moskaleva and M. C. Lin, *J. Phys. Chem. A*, 2001, **105**, 4156.
21. R. Pd and P. Chandra, *J. Chem. Phys.*, 2001, **114**, 1589.
22. V. V. Melnikov and P. Jensen, *Chem. Phys. Lett.*, 2004, **394**, 171.
23. T. V. Alves, Y. Alexandre Aoto and F. R. Ornellas, *Mol. Phys.*, 2010, **108**, 2061.
24. T. J. Frankcombe, S. D. NcNeil and G. Nyman, *Chem. Phys. Lett.*, 2011, **514**, 40.
25. J. Ma, H. Guo and R. Dawes, *Phys. Chem. Chem. Phys.*, 2012, **14**, 12090.
26. E. M. Goldfield, S. K. Gray and L. B. Harding, *J. Chem. Phys.*, 1993, **99**, 5812.
27. M. H. Alexander, D. E. Manolopoulos and H.-J. Werner, *J. Chem. Phys.*, 2000, **113**, 11084.
28. M. H. Alexander, G. Capecchi and H.-J. Werner, *Faraday Disc.*, 2004, **127**, 59.
29. H. Lefebvre-Brion and R. W. Field, *Perturbations in the Spectra of Diatomic Molecules*. Academic Press, Orlando, 1986.
30. Z. Sun, D. H. Zhang and M. H. Alexander, *J. Chem. Phys.*, 2010, **132**, 034308
31. H. J. Werner, P. J. Knowles, G. Knizia, F. R. Manby and M. Schütz, *WIREs Comput. Mol. Sci.*, 2012, **2**, 242.
32. H.-J. Werner and P. J. Knowles, *J. Chem. Phys.*, 1985, **82**, 5053.

33. P. J. Knowles and H.-J. Werner, *Chem. Phys. Lett.*, 1985, **115**, 259.
34. K. A. Peterson, T. B. Adler and H.-J. Werner, *J. Chem. Phys.*, 2008, **128**, 084102.
35. T. Shiozaki and H.-J. Werner, *Mol. Phys.*, 2013, **111**, 607.
36. B. Jiang and H. Guo, *J. Chem. Phys.*, 2013, **139**, 054112.
37. J. Li, B. Jiang and H. Guo, *J. Chem. Phys.*, 2013, **139**, 204103.
38. B. J. Braams and J. M. Bowman, *Int. Rev. Phys. Chem.*, 2009, **28**, 577.
39. B. Jiang, J. Li and H. Guo, *Int. Rev. Phys. Chem.*, 2016, **35**, 479.
40. H. Guo, *Rev. Comput. Chem.*, 2007, **25**, 285.
41. D. T. Colbert and W. H. Miller, *J. Chem. Phys.*, 1992, **96**, 1982.
42. J. V. Lill, G. A. Parker and J. C. Light, *J. Chem. Phys.*, 1986, **85**, 900.
43. J. C. Light and T. Carrington Jr., *Adv. Chem. Phys.*, 2000, **114**, 263.
44. H. Tal-Ezer and R. Kosloff, *J. Chem. Phys.*, 1984, **81**, 3967.
45. S. Y. Lin and H. Guo, *Phys. Rev. A*, 2006, **74**, 022703.
46. J. M. Bowman, *J. Phys. Chem.*, 1991, **95**, 4960.
47. D. H. Zhang and J. Z. H. Zhang, *J. Chem. Phys.*, 1999, **110**, 7622.
48. K. M. Hickson, J.-C. Loison, H. Guo and Y. V. Suleimanov, *J. Phys. Chem. Lett.*, 2015, **6**, 4194.
49. K. Haris and A. Kramida, *Astrophys. J. Suppl. Ser.*, 2017, **233**, 16.
50. A. Beckmann, K. D. Böklen, G. Bremer and D. Elke, *Z. Phys. A*, 1975, **272**, 143.

Table I. The electronic Hamiltonian in the six-state diabatic basis.

$\hat{H}_{el}$	$\left\|{}^3\Pi_1;+1\right\rangle$	$\left\|{}^1\Delta_2;0\right\rangle$	$\left\|{}^3\Pi_{-1};-1\right\rangle$	$\left\|{}^1\Delta_{-2};0\right\rangle$	$\left\|{}^3\Pi_1;-1\right\rangle$	$\left\|{}^3\Pi_{-1};+1\right\rangle$
ω	2	2	-2	-2	0	0
$\left\|{}^3\Pi_1;+1\right\rangle$	V_Π	0	0	0	0	V_1
$\left\|{}^1\Delta_2;0\right\rangle$	0	V_Δ	0	V_2	0	0
$\left\|{}^3\Pi_{-1};-1\right\rangle$	0	0	V_Π	0	V_1	0
$\left\|{}^1\Delta_{-2};0\right\rangle$	0	V_2	0	V_Δ	0	0
$\left\|{}^3\Pi_1;-1\right\rangle$	0	0	V_1	0	V_Π	0
$\left\|{}^3\Pi_{-1};+1\right\rangle$	V_1	0	0	0	0	V_Π

Table II. The SO Hamiltonian in the six-state diabatic basis.

$\hat{H}_{so}$	$\left\|{}^3\Pi_1;+1\right\rangle$	$\left\|{}^1\Delta_2;0\right\rangle$	$\left\|{}^3\Pi_{-1};-1\right\rangle$	$\left\|{}^1\Delta_{-2};0\right\rangle$	$\left\|{}^3\Pi_1;-1\right\rangle$	$\left\|{}^3\Pi_{-1};+1\right\rangle$
ω	2	2	-2	-2	0	0
$\left\|{}^3\Pi_1;+1\right\rangle$	A	C	0	0	0	0
$\left\|{}^1\Delta_2;0\right\rangle$	C	0	0	0	0	0
$\left\|{}^3\Pi_{-1};-1\right\rangle$	0	0	A	$-C$	0	0
$\left\|{}^1\Delta_{-2};0\right\rangle$	0	0	$-C$	0	0	0
$\left\|{}^3\Pi_1;-1\right\rangle$	0	0	0	0	E	0
$\left\|{}^3\Pi_{-1};+1\right\rangle$	0	0	0	0	0	E

Table III. Total Hamiltonian in a two-state model.

$\hat{H}_{so}+\hat{H}_{el}$	$\left\vert {}^3\Pi_{\pm1};\pm1\right\rangle$	$\left\vert {}^1\Delta_{\pm2};0\right\rangle$
ω	±2	±2
$\left\vert {}^3\Pi_{\pm1};\pm1\right\rangle$	$V_{\Pi}+A$	$\pm C$
$\left\vert {}^1\Delta_{\pm2};0\right\rangle$	$\pm C$	V_{Δ}

Table IV. Calculated equilibrium geometries of the collinear CNN radical

State	This Work		Hickson *et al*.[15]	
	r(C-N) /Å	*r*(N-N) /Å	*r*(C-N) /Å	*r*(N-N) /Å
$\tilde{A}^3\Pi$	1.223	1.183	1.226	1.178
$a^1\Delta$	1.261	1.183	1.262	1.185
$\tilde{X}^3\Sigma^-$	1.235	1.208	1.249	1.183

Table V. Adiabatic excitation energies for the ground state CNN radical and comparison with experiment.

State	Excitation energies /cm^{-1}			
	This work w/ ZPEs	Hickson *et al.*[15] w/o ZPEs	Pd *et al.*[21] w/ ZPEs	Expt.[18]
$\tilde{A}^3\Pi$	24017	23825	23850	23850
$a^1\Delta$	6798	6803	7879	6823±113

Table VI. Calculated fine-structure energies for the ground state carbon atom using the ab initio (scaled) SO couplings in comparison with experimental values.

C	This work/cm^{-1}	Expt. /cm^{-1} [49, 50]
$^3P_0$	0	0
$^3P_1$	12.64(15.33)	16.42
$^3P_2$	37.87(45.94)	43.41

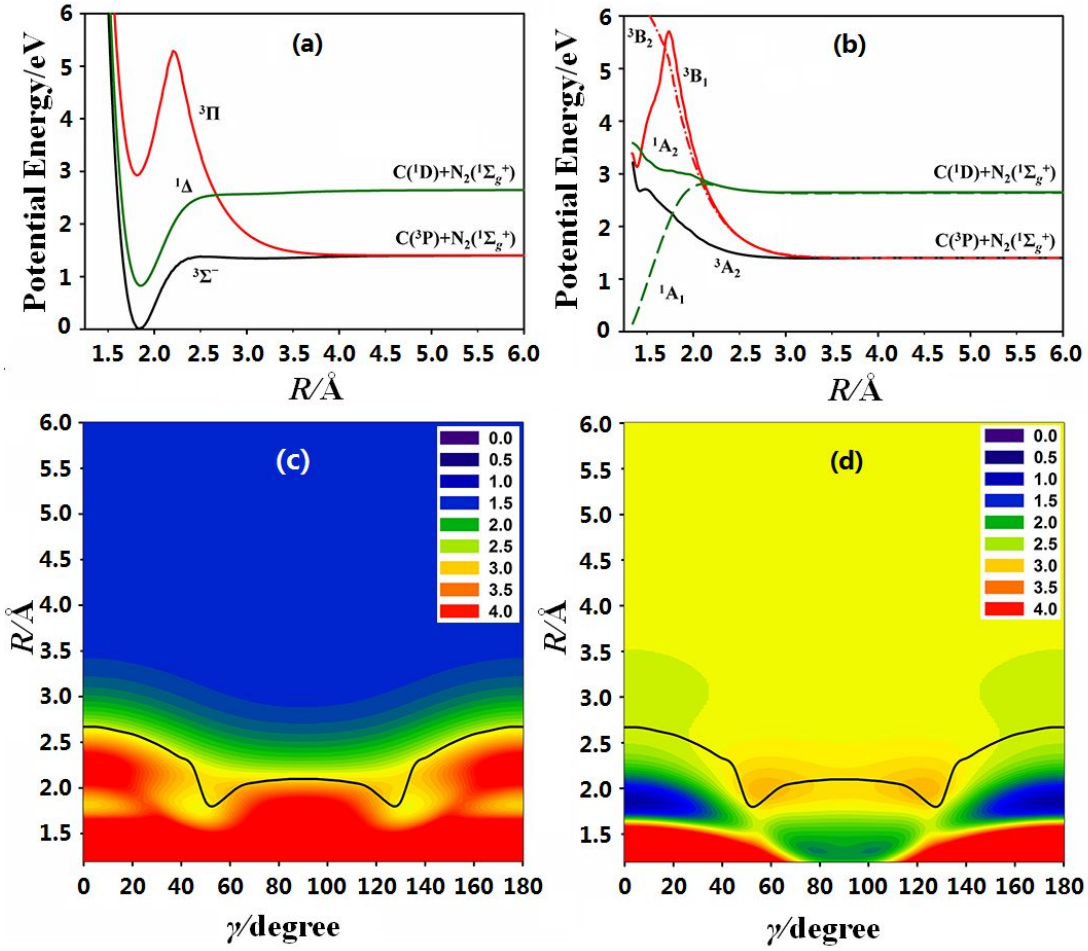

FIG. 1. Potential energy curves of the ground and low-lying excited states of the C + N_2 collisions in collinear (a) and perpendicular (b) approaches. For each distance R, the r(N-N) distance is optimized. Contour plots of the adiabatic PESs averaged over the two triplet states $2^3A''$ and $1^3A'$ (c) and two singlet states $1^1A'$ and $1^1A''$ (d) are plotted as a function of R and γ. The distance r(N-N) is optimized for each (R, γ). The contour intervals are 0.5eV. The crossing seam between the triplet and singlet adiabatic PESs is illustrated by a solid black line.

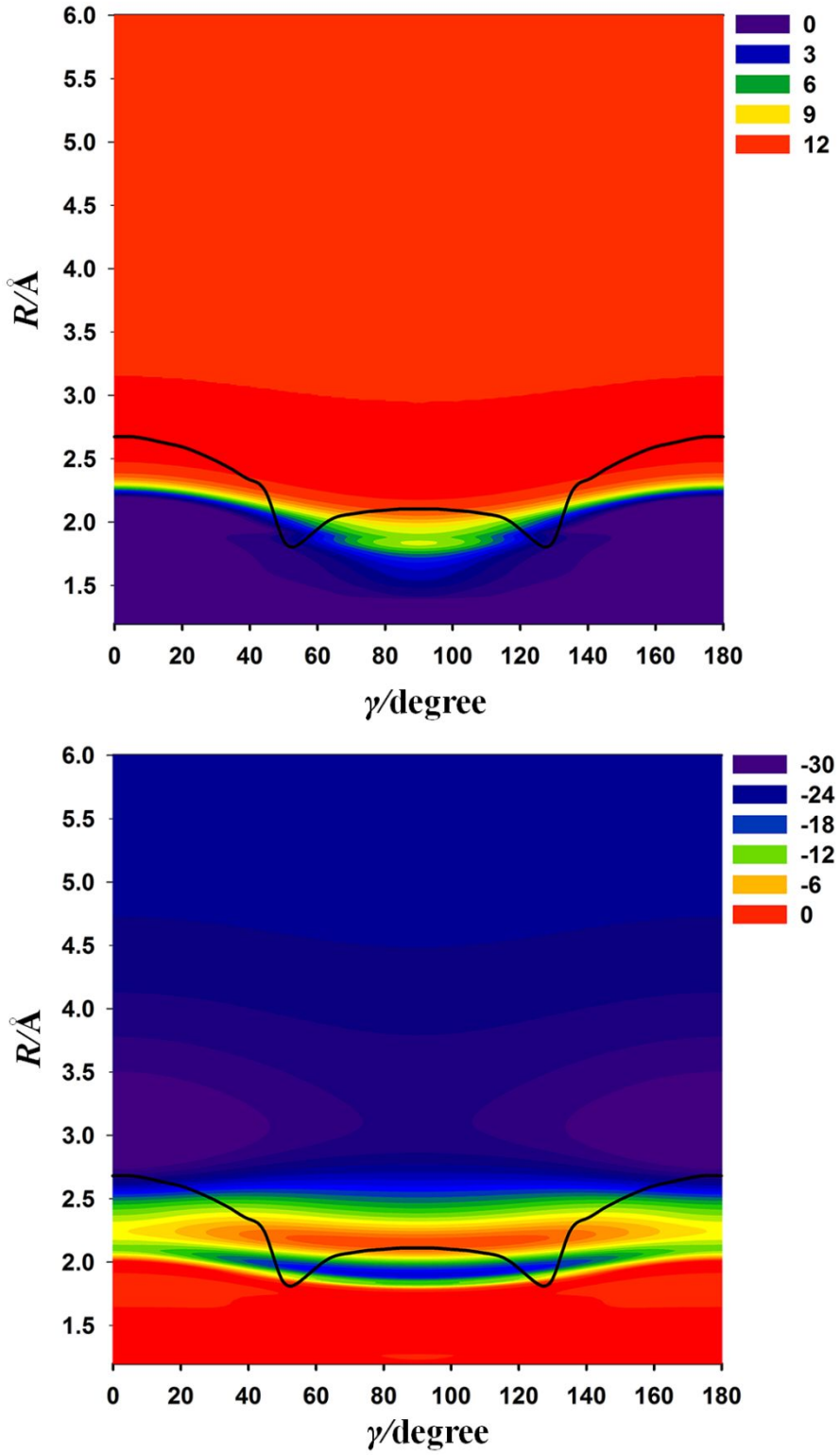

FIG. 2. Contour plots of the SO coupling elements A (upper panel) and C lower panel (cm^{-1}) as a function of (R, γ) with the r(N-N) distance fixed at 1.183 Å. The contour starts as 0 cm^{-1} with an interval of 3 cm^{-1} for A and 6 cm^{-1} for C.

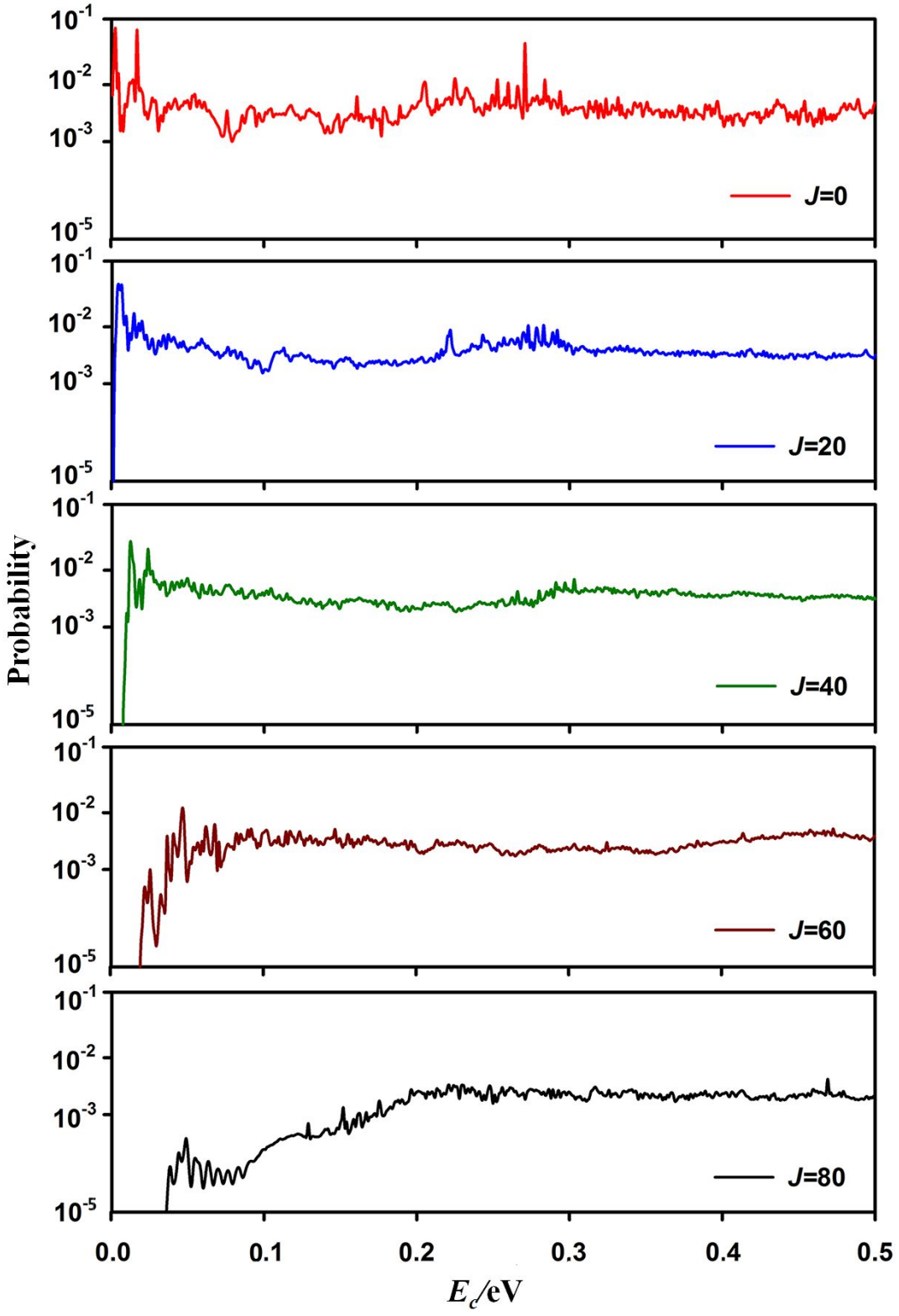

FIG. 3. Quenching reaction probabilities of $C(^1D)+N_2(v, j=0) \rightarrow C(^3P)+N_2(v', j')$ as a function of the collision energy (E_c) for several partial waves.

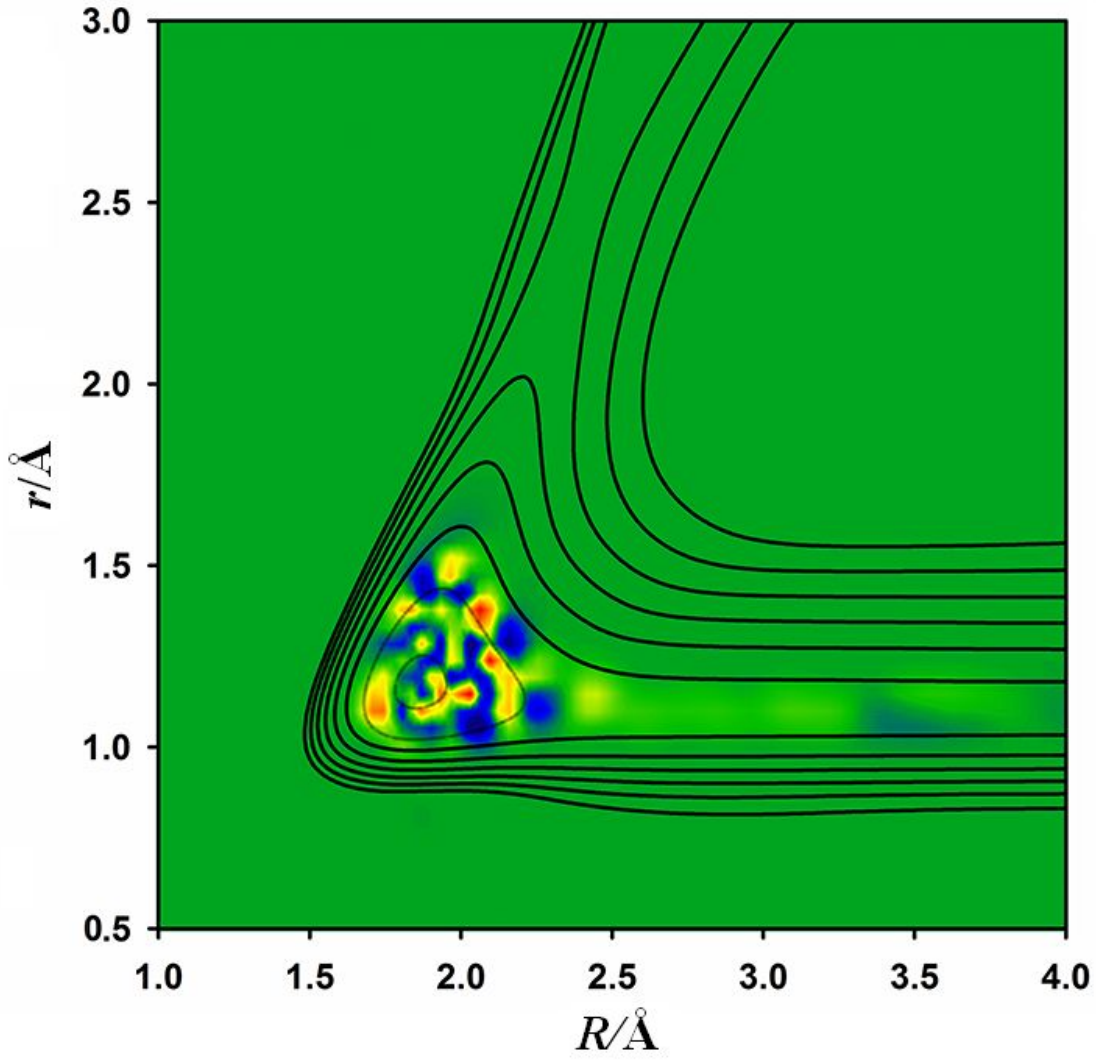

FIG. 4. Contour of the $^1\Delta$ component of a resonance wavefunction (J=0) at 0.284 eV of collision energy overlaid on the PES of the $^1\Delta$ state. The Jacobi angle is fixed at 0.

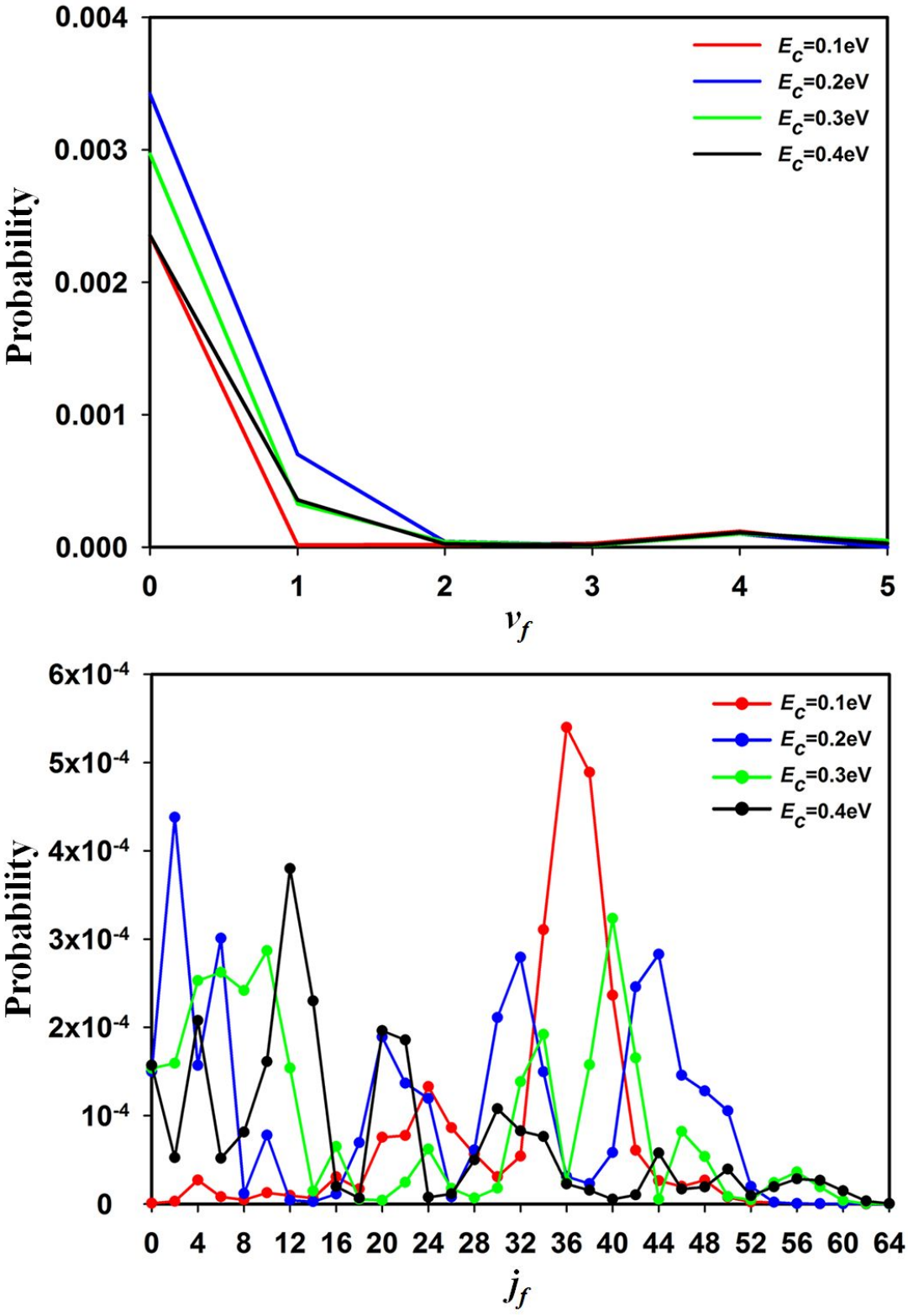

FIG. 5. The J=0 N_2 vibrational (upper panel) and rotational (v_f=0, lower panel) state distributions for several collision energies (E_c).

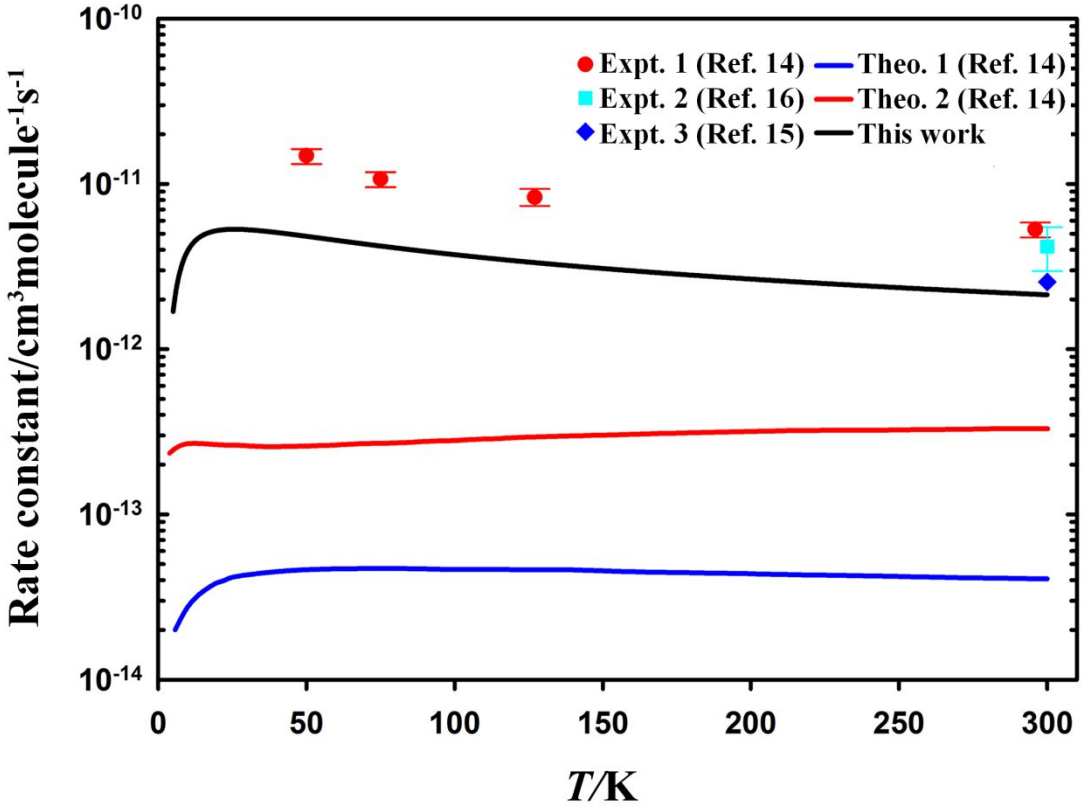

FIG. 6. Rate constants for the $C(^1D)+N_2(v, j=0) \rightarrow C(^3P)+N_2(v', j')$ quenching reaction as a function of temperature. Expt. 1-3 are data from Hickson *et al.*[15] (red circle), Husain *et al.*[17] (cyan square) and Braun *et al.*[16] (blue diamond). The rate coefficient calculated in this work (black line) is much closer to the experimental data than those obtained with the collinear (red line) and spherical (blue line) models.[15]

TOC graphic